Hindawi
International Journal of Photoenergy
Volume 2018, Article ID 1308381, 10 pages
https://doi.org/10.1155/2018/1308381

Research Article

Rapid, Chemical-Free Generation of Optically Scattering Structures in Poly(ethylene terephthalate) Using a CO_2 Laser for Lightweight and Flexible Photovoltaic Applications

Simon D. Hodgson and Alice R. Gillett

Department of Mechanical Engineering, University of Chester, Chester, UK

Correspondence should be addressed to Simon D. Hodgson; s.hodgson@chester.ac.uk

Received 31 July 2018; Revised 15 November 2018; Accepted 22 November 2018; Published 16 December 2018

Academic Editor: Yanfa Yan

Highly light scattering structures have been generated in a poly(ethylene terephthalate) (PET) film using a CO_2 laser. The haze, and in some cases the transparency, of the PET films have been improved by varying the processing parameters of the laser (namely, scanning velocity, laser output power, and spacing between processed tracks). When compared with the unprocessed PET, the haze has improved from an average value of 3.26% to a peak of 55.42%, which equates to an absolute improvement of 52.16% or a 17-fold increase. In addition to the optical properties, the surfaces have been characterised using optical microscopy and mapped with an optical profilometer. Key surface parameters that equate to the amount and structure of surface roughness and features have been analysed. The CO_2 laser generates microstructures at high speed, without affecting the bulk properties of the material, and is inherently a chemical-free process making it particularly applicable for use in industry, fitting well with the high-throughput, roll to roll processes associated with the production of flexible organic photovoltaic devices.

1. Introduction

The photovoltaic (PV) industry is both incredibly valuable and growing rapidly. In 2017, more capacity was added from solar PV than any other technology and can be considered amongst the leading contenders for replacing fossil fuels as the major provider of energy worldwide [1]. Traditional first-generation solar cells have reached efficiencies of 26.7%, very close to the theoretical maximum of ~33% [2, 3]. Thin-film PV, also known as second-generation PV, has closed the gap significantly in recent years. The two dominant technologies are cadmium telluride (CdTe) and copper indium gallium diselenide (CIGS) which have verified records of 21.0% (with the standard active area of $\geq 1\,cm^2$, at active areas below this, the record is 22.1%) and 22.9%, respectively [2]. Thin-film PV is designed using materials that have very high absorption coefficients. This enables the devices to have absorber layer thicknesses of the order of $\sim 10\,\mu m$ and below, a considerable material saving over the 100–500 μm thick active layers in first-generation PV [4]. Third-generation PV (3GPV) covers a broad area of different technologies. 3GPV primarily focuses on overcoming the Shockley-Queisser limit through the application of one or more methods such as hot-carrier absorption, photon management techniques, multiple p-n junctions, and concentration [5–8]. Despite this, many novel new material types are also classed as 3GPV. This includes dye-sensitised (DSC), organic (OPV), and perovskite-based devices [9–11]. These new technologies offer the potential for even lower production costs and have applications to a range of niche markets otherwise inaccessible to classic module design. Of these, perovskites have the highest recorded efficiency of 20.9% to date (standard active area, 22.7% on smaller) [2, 12]. One advantage of these new technologies is the ability to be deposited on polymer substrates. This is particularly the case for OPV, something that not only provides a reduction in cost, but allows devices to be flexible [13].

The engineering of structures at the micro- and nanoscale to increase the photon collection of PV cells is well established. These have found particular application to

thinner absorber materials where maximising the absorption over a small optical path length is key to increasing performance. The structures range from the texturing of surfaces to reduce reflection (e.g., through the generation of black silicon and similar structures or through the creation of both ordered and randomly generated structures designed to create a high degree of light scattering (also known as haze) or induce light trapping) [14–16]. Another route used to increase photon capture is the application of plasmonic layers [17]. The methods used to create these types of surfaces revolve around either the growth of structures on top of a PV layer (e.g., through PVD- or CBD-based methods) or through the removal of material to create the structures (i.e., etching) [18, 19]. In nearly all cases, additional and normally highly toxic chemicals are needed as reaction precursors, or as part of an etching process. Laser processing, by contrast, is normally free of the use of toxic material beyond the use of common solvents for cleaning [20]. Lasers have been used in many fields. These range from a machining tool in cutting and welding applications [21] to the engineering of surfaces in biomedical or orthopaedic applications [22, 23], as well as microfluidics and as a part of the deposition of thin films [24, 25]. Carbon dioxide (CO_2) based lasers are amongst the most well-used systems today. They are fairly efficient, low in cost, and highly flexible for use in a range of applications. CO_2 lasers are the highest power continuous wave systems around and are also q-switchable to yield very high power densities per pulse [26–28].

Poly(ethylene terephthalate) (PET) is a common polymer that is used in food packaging, in medical devices, and in PV as either a substrate or as part of the encapsulation of a module [29–32]. It is low in cost, lightweight and has good mechanical and optical properties [29]. This work presents the first steps towards the development of a chemical-free (beyond the initial clean) CO_2 laser-based process to engineer a PET layer for the production of light scattering structures designed to increase the performance of flexible PV devices at high speeds.

2. Materials and Methods

2.1. Surface Engineering. The CO_2 laser system used was a 60 W Synrad Firestar system fitted with a galvanometric scanning head producing a FWHM spot size of 171 μm. Each sample was produced as a series of parallel lines in a 10 mm^2 area. Three processing parameters have been varied throughout the set of experiments. These are the laser power, scanning speed, and the line spacing. The parameters were set according to Table 1, with every possible combination tested, resulting in a total of 64 samples created. Prior to experimentation, the laser power was measured using a Mahoney laser power probe. The measured values have been included in Table 1 next to the percentage power used. The transparent 0.25 mm thick a-PET film was purchased from Goodfellows Inc., and prior to laser treatment, samples were briefly cleaned with isopropyl alcohol wipes to remove surface contamination and minimise additional solvent use. All processing was performed in ambient air.

Table 1: The range of setting sued for laser engineering structures onto the PET surface. Every combination was tested, resulting in 64 total sample types.

Laser power (%)	Scanning speed (mm/s)	Line spacing (μm)
5 (3.75 W)	100	300
10 (6.33 W)	200	400
15 (11.25 W)	300	500
20 (14.67 W)	400	600

2.2. Surface Characterisation. Two types of surface characterisation have been performed: surface profilometry and optical microscopy. Surfaces have been mapped using a STIL Micromeasure 2 confocal chromatic imager (CCI). An area of 1×1 mm was scanned on each sample with a step size of 10 μm. Data processing was done using MountainMaps software, and all raw data was comparably filtered and processed. Multiple 3D surface parameters have been calculated and analysed, namely, S_a (arithmetic mean roughness), S_z (10-point height), S_{ku} (kurtosis of height distribution), and S_{sk} (skewness of height distribution). Optical microscopy was performed on a Leica DM2700 microscope.

2.3. Optical Measurements. An Ocean Optics QE-Pro series UV-VIS spectrometer has been used to measure the optical properties of the laser-processed PET samples. All samples, including an unprocessed as-received (AR) sample, were measured using an integrating sphere. Two reference measurements have been taken: T_1, the equivalent to 100% transmission, and T_3, identical to T_1 with the exit port of the integrating sphere open to allow the direct beam of light to pass through the sphere so only stray light from the natural bloom of the beam is detected. For each sample, two further measurements have been taken. These are T_2, the equivalent to T_1 but with the sample in place, and T_4, the equivalent to T_3 with the sample in place. Equation 1 can then be used to calculate the total transmission (T_T) of each sample, equation 2 can be used to calculate the diffuse transmission (T_d), and equation 3 can be used to calculate the total haze (T_H).

$$T_T = \frac{T_2}{T_1}, \tag{1}$$

$$T_d = \frac{T_4 - T_3(T_2/T_1)}{T_1}, \tag{2}$$

$$T_H = \frac{T_d}{T_T}. \tag{3}$$

3. Results and Discussion

3.1. Surface Analysis. Analysis of the surfaces produced shows a range of different structures produced on the PET samples. Interestingly, two of the samples, both processed at 20% power and 100 mm/s scanning speed whilst having spacings of 300 and 400 μm, respectively, caused the samples to melt through, resulting in their destruction due to power densities greater than the PET being able to withstand.

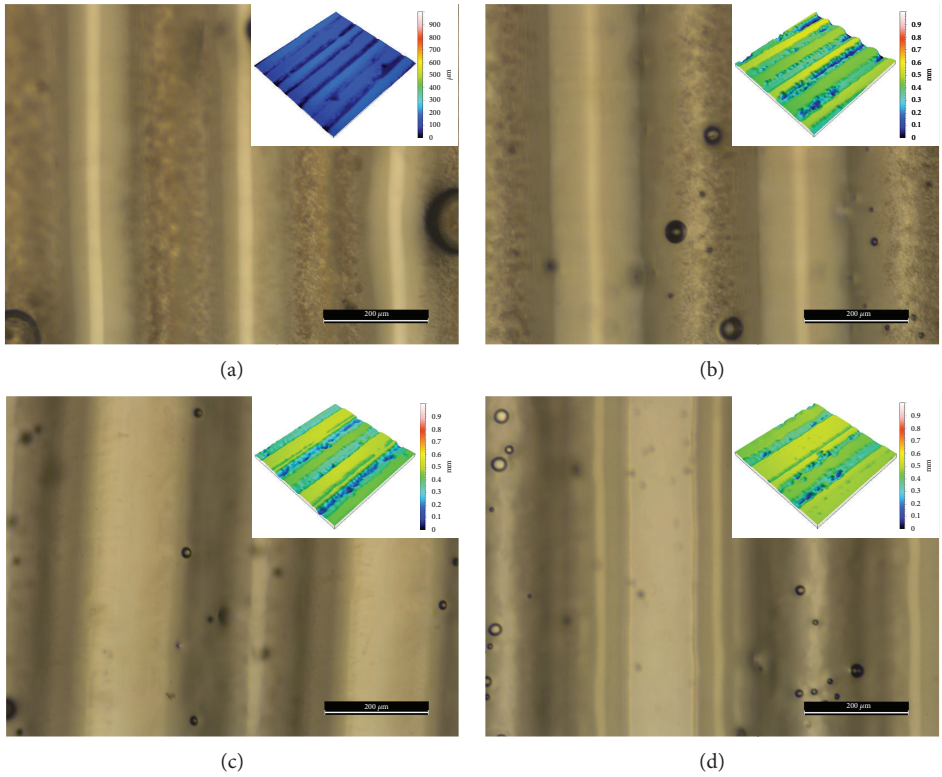

Figure 1: Optical micrographs of 4 laser-processed PET samples with increasing spacing between the parallel laser processing lines. (a) 300 μm; (b) 400 μm; (c) 500 μm; (d) 600 μm. All samples have been processed at 15% power and a scanning speed of 200 mm/s. The insets are CCI surface maps that have been set to the same z scale, and horizontally the scale bar is equal to 200 μm.

Optical microscopy of the samples demonstrates in detail the structure of the surfaces. Figure 1 displays a series of samples with increasing spacing from 300 to 600 μm. In each image, the power and scanning speed are constant. As would be expected, the wider the spacing, the greater the area of AR-like material. Some bubbling is visible in the samples, caused by air becoming trapped in molten PET as it cools rapidly following laser processing. From the CCI surface maps, it can be observed that the sample with the smallest spacing has a smaller z range than the wider-spaced samples. This has been caused by heat transfer within the sample from successive line scans that are in close enough proximity to affect the previous scan. Here, the effect is to reduce the effective depth of the process by remelted PET partly filling any trenches previously engraved in the surface. The FWHM of the laser yields a spot size of 171 μm, which is the equivalent of a $1/e^2$ spot size of 290 μm. As polymers do not resist heat particularly effectively, it can be seen that the proposed remelting effect is likely occurring due to spot size and spacing (for the smallest spacing) being similar in scale. Once the spacing reaches a sufficiently wide level, this effect reduces and disappears. By analysing the surface roughness data further, support for this is found. By averaging the S_a, S_z, S_{sk}, and S_{ku} for all the samples with the same spacing, we find that the average roughness (S_a) increases as spacing increases. The 300 μm spacing displays an average roughness of ~10.8 μm which increases to 12.8 μm by 600 μm spacing. 400 and 500 μm spacing samples have comparable values. S_a alone is a comparatively useless value, however, as samples with a large z range and a small z range can have a similar average roughness despite vastly different surfaces. Comparing S_a with S_z provides a better demonstration of the scale of the surface roughness. S_z gives a measure of the scale of surface roughness, i.e., from the lowest valleys to the highest peaks. The same trend is observed, showing that not only does the average roughness of the samples increase so but also does the scale of the roughness. There is approximately a 100 μm increase in surface roughness from 300 to 600 μm spacing. Other key parameters, S_{sk} and S_{ku}, also provide useful information about the roughness features on the surface. S_{sk} is the skewness of the surface and relates to the relative dominance of peaks or valleys in the surface. S_{ku} is the kurtosis and is an indication of how high or not the peaks and valleys are. Both S_{sk} and S_{ku} are unitless. All the sample spacings demonstrate a negative skewness, indicating a predominance of valleys. This would be expected as laser processing is typically an ablative removal process that generates valleys. There is a slightly larger average negative skewness value for 300 μm spacing (−1.60), vs. the increasing spacing (−1.51, −1.43, and −1.33, respectively). Whilst the values are, of course, close, one explanation could be due to increasing spacing resulting in a relative decrease in the volume of processed area—reducing the relative amount of valleys. S_{ku} values demonstrate an increase in the lowest level of kurtosis—meaning the lower level of deep valleys—for the smallest spacing. This increases from 8.2 to 9.8 and 9.4 for 400 and

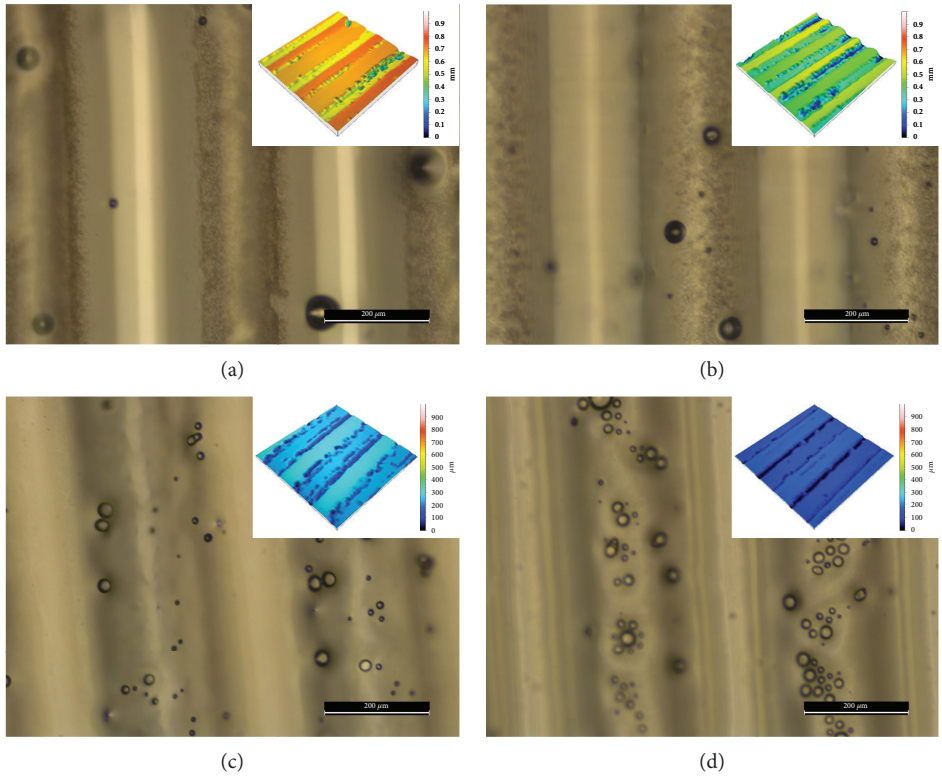

Figure 2: Optical micrographs of 4 laser-processed PET samples with increasing scanning speed between the parallel laser processing lines. (a) 100 mm/s; (b) 200 mm/s; (c) 300 mm/s; (d) 400 mm/s. All samples have been processed at 15% power and at 400 μm spacing. The insets are CCI surface maps that have been set to the same z scale, and horizontally the scale bar is equal to 200 μm.

500 μm spacings, very similar values, and then 10.2 for the largest spacing. This would seem to support the idea of a remelt at lower spacings causing some of the depth of process to be removed. This also explains the reduced number of bubbles within the 300 μm spaced sample, due to slower cooling rates (caused by the remelting) allowing more trapped air to escape the sample.

Figure 2 shows optical micrographs illustrating the impact of scanning speed on the surface of PET. Scanning speed ranges from 100 to 400 mm/s. All other parameters have been held constant. Interestingly, at faster scanning speeds there appears to be an increase in air bubbles trapped within the polymer. The likely explanation for this is that due to the faster scanning speeds resulting in less laser power per second striking an area of the surface, that whilst providing sufficient energy to process the PET, the temperature the PET reaches will likely be lower. This would result in an increase in the speed any molten polymer cools at, reducing the likelihood of any trapped air escaping. From the CCI images, it can be observed that the z scale of the surfaces decreases with increasing speed. Again, this relates to the laser power per second striking a surface. The longer the laser beam interacts with a spot on the surface, the greater the level of melting and ablation that occurs. Indeed, it can also be seen on the optical micrographs that the laser tracks appear to be significantly deeper at 100 mm/s than at 400 mm/s where there is comparatively little surface processing. Analysis of the roughness data supports this. Whilst the average roughness shows no particular trend, the S_z of 100 mm/s is the largest (252 μm), with 300 and 400 mm/s showing the lowest values (165 and 192 μm). S_{sk} shows negative values for all samples, with the greater negative skewness, indicating a higher proportion of valleys, at the slowest scanning speeds. Again, the S_{ku} supports the theory of slower speeds yielding deeper valleys, with the average S_{ku} of 100 mm/s samples being over 12, whilst for all other speeds it is less than 10.

Figure 3 contains optical micrographs displaying the impact of laser processing power on PET surfaces. Laser powers range from 5 to 20%; all other parameters have been held constant. At a laser power of 5%, very little impact has been observed on the surface, whereas at higher powers tracks are visible. Bubbling is observed significantly at 10% power, a small amount at 15% power, and not at all at 20%. This relates to the aforementioned higher power per second causing hotter melted PET resulting in a longer cooling time allowing air pockets time to escape. There is no significant bubbling at 5% power due to the limited laser material interaction taking place. As demonstrated in the CCI maps, the width and depth of engraving increase significantly with laser power. The average of the mean and scale of the surface roughness is at its lowest for 5% power ($S_a = 9.5\mu$m, $S_z = 132\mu$m), compared to the other samples which all exhibit S_a values > 10.7μm, and S_z values > 210 μm. The average skewness and kurtosis of the 5% power processed samples are also significantly lower, indicating fewer and smaller valleys being created in the PET surface

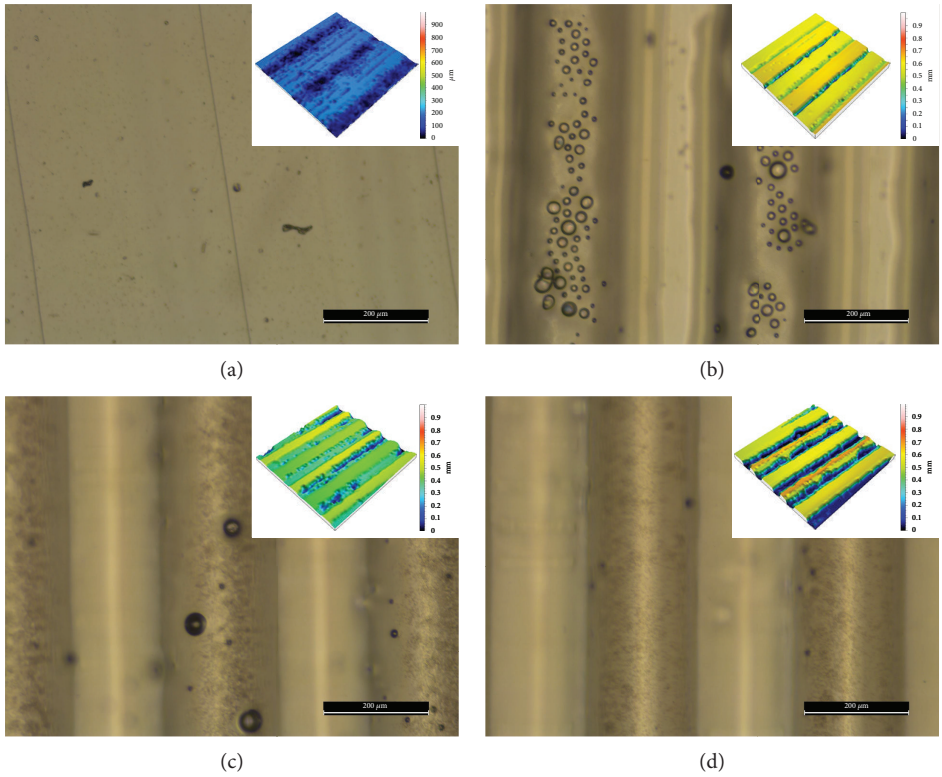

Figure 3: Optical micrographs of 4 laser-processed PET samples with increasing laser power. (a) 5%; (b) 10%; (c) 15%; (d) 20%. All samples have been processed at a scanning speed of 200 mm/s and at 400 μm spacing. The insets are CCI surface maps that have been set to the same z scale, and horizontally the scale bar is equal to 200 μm.

of the 5% sample which are −0.77 and 6.0, respectively. The other powers all exhibit an S_{sk} of <−1.45 and S_{ku} of >10.0. The caveat with all of these averaged roughness values is that each parameter has its own individual effect, which can confound other results. Despite this, there are visible trends and observations from this data that make sound logical sense when considering how an infrared laser interacts with PET.

3.2. Optical Properties. After characterising the surfaces of the samples, the optical properties have been measured. Considering the location of the PET layer in the PV cell, as either a substrate or part of the encapsulation system, and therefore incident to the incoming light, the two most important properties are the transmissivity, i.e., how much of the incoming light will pass through to the device, and the haze, i.e., how much the light is scattered. PET has a refractive index of ~1.57, which yields an approximate reflection loss of around 4–5% per surface interface. For analysis of the optical data, a wavelength range between 400 and 750 nm has been selected, although longer was measured. This range coincides with the majority of photon energy available to all PV active materials for absorption not only for the most common semiconductor materials, i.e., silicon, CdTe, and CIGS, but also and more importantly for the target PV materials for this light scattering technology, OPV and perovskites which often do not absorb towards the near-infrared [2]. Laser processing the samples appears to have a small impact on the transmissivity of the PET when compared to the AR sample. Figure 4(a) displays the average transmission of samples as a function of laser parameter, whereas Figure 4(b) displays example transmission spectra of the AR PET sample and compares it to the sample that produced the highest haze value. In Figure 4(a), the values for each run with a particular setting have been averaged, in order to view the effect that a particular parameter shows. Many of the settings show a slight increase in transmission, ~1–2%. This could be because of two primary reasons. The first is that due to material removal due to the laser-material interaction. Less material will cause a slight reduction in absorption. However, due to the very low absorption that occurs within PET at these wavelengths, this would appear to have minimal impact. Another possibility is that the surface structures are acting in some way to partially trap light. The textured surface is nonflat, which allows for an increase in total internal reflection due to the change in angle of incidence relative to the surface. Another possibility is a pseudolensing effect caused by the regular ray of structures that have been created that may partially concentrate the light at a very small scale. Perhaps the most interesting effect is that of changing laser power on the transmissivity of the PET film. The lowest laser power demonstrates an average transmission value equivalent to that of the unprocessed PET, whereas the higher powers all display a slight increase to transmission. This would imply that at the lowest power, any structures created on the surface are comparatively small and having a minimal effect on the incident light.

Figure 5 shows the average haze of laser-processed PET films, again averaged between the wavelength range of 400–750 nm. The laser processing has generated impressive levels

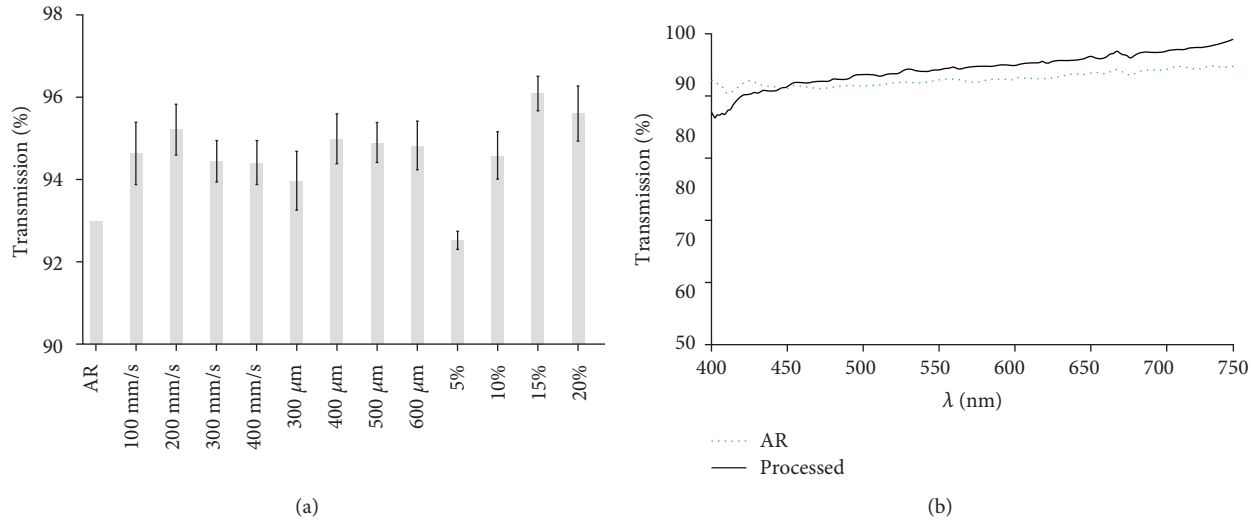

Figure 4: (a) The averaged transmission values from 400 to 750 nm for each of the laser parameters tested and the unprocessed AR sample. The error bars show the standard error of the mean. (b) A comparison between the transmission spectra of the as-received PET sample and those of the sample that produced the highest haze.

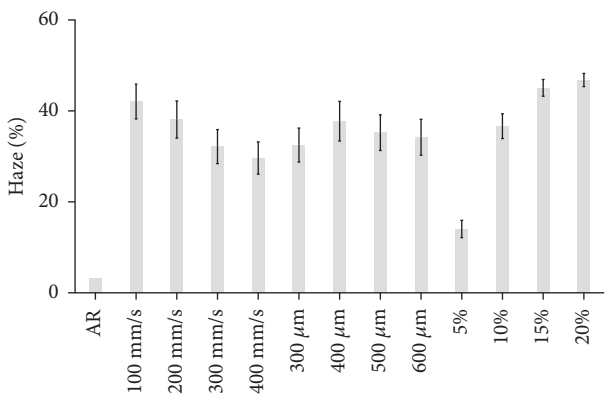

Figure 5: The averaged haze from 400 to 750 nm for each of the laser parameters tested and the unprocessed AR sample. The error bars show the standard error of the mean.

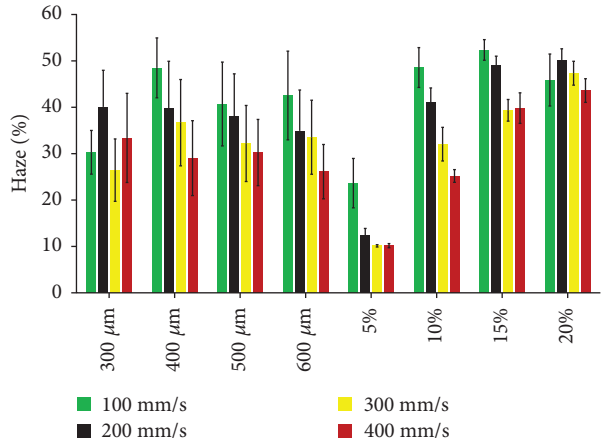

Figure 6: The averaged haze from 400 to 750 nm as a function of the scanning speed. The colours relate to the results separated by processing speed: green: 100 mm/s, black: 200 mm/s, yellow: 300 mm/s, and red: 400 mm/s. The error bars show the standard error of the mean.

of haze in the PET film. The AR PET has a very low level of native haze, ~3%, whereas the laser-engineered surfaces, in some cases, exhibit average haze levels in excess of 50%. Evaluating the light scattering properties of the laser-textured films also suggests that the power of the beam is the most important property for generating high haze surfaces. As the laser power increases, there appears to be a clear trend towards increased average haze. A deeper analysis is required, however, as laser parameters often have a similar effect. In particular (and as discussed previously), the scanning speed also heavily affects the power density per unit time of a laser, with a slower scanning speed resulting in a greater effective power density hitting a single spot. This is also visible to an extent in the haze levels produced.

Figure 6 shows the average haze of the PET films as a function of the laser scanning speed. It has previously been observed in this paper that the slower the scanning speed, the greater the feature, and thus the greater the scattering; however, this can confound the effect of the laser power on the haze. At the slowest scanning speed, 100 mm/s, the average haze of the lowest power, 5%, is at its highest. The haze levels of the other three powers are very comparable at this speed, suggesting possibly the upper limit in the amount of haze creatable in these films by this method. As the scanning speed increases, the haze at a power of 5% decreases dramatically from >20% to <10%. Laser powers of 10% and 15% show their highest total haze values at the slowest scanning speed, with decreasing average haze as speed increases. However, at the highest power the levels of Haze remain quite constant. The line spacing of the samples appears to have limited effect on the haze of the sample once the spacing is sufficient to limit the effect of subsequent process lines on prior ones. The highest haze value obtained in this work is

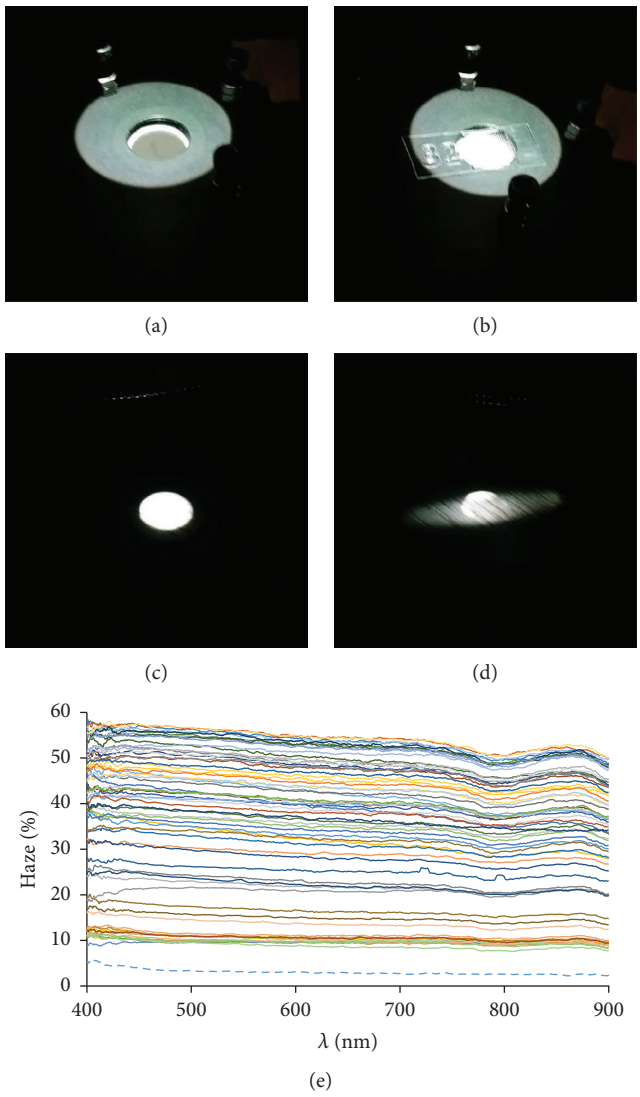

Figure 7: (a–d) Photographs showing the directional scattering caused by the laser-processed PET (b, d) relative to having no sample (a, c). The sample used for this image has a speed of 400 mm/s, a spacing of 400 μm, and a power of 20%. The average haze (400–750 nm) is 43.5%. The graph displays the measured haze of all 64 samples and demonstrates the range of haze values created. The dashed line in (e) is the AR sample.

from a sample with 100 mm/s scanning speed, 400 μm spacing and a power of 15% (the equivalent sample with 20% power was one of the two that destroyed the sample).

Another interesting observation is that of the highly directional scattering of light by the high haze structures. Figure 7 displays photographs showing unscattered light compared with the presence of a structured PET film. Instead of a wider circle of light leaving the integrating sphere, which would indicate uniform scattering in both the x and y directions, the light is scattered perpendicular to the directions of the laser marks. This is intriguing and gives the potential for combinations of differentially orientated structures to maximise light scattering effects. The haze measurements for all the samples can also be observed in Figure 7, demonstrating the range of Haze values created by varying only three parameters. It should be noted that there is no consistent trend between the roughness values and the overall Haze. This would suggest that the light scattering is dependent on the production of features and patterning rather than microroughness alone.

3.3. Potential for Enhancing Photovoltaics and the Advantages of Laser Processing. Laser-structured PET clearly has the ability to improve the efficiency of solar cells by utilising light scattering mechanisms. The increased haze is comparable to many high haze films that have been demonstrated to increase some cell efficiencies by over 10% [33–36]. The advantages in the process described in this paper have already been discussed somewhat in the introduction; however, they bear repeating when combined with the discoveries within this work. The laser process is, most importantly for any industrial process, very fast. Films demonstrating up to 50% haze have been generated at scanning speeds of 400 mm/s using laser powers that are very low considering that CO_2 lasers in the kW levels of power output are commonly available. This leads to the chance of significantly faster processing speeds to counteract the possible power increases and certainly at levels sufficient to be incorporated as part of any batch or roll-to-roll process. This is particularly important as roll-to-roll production is one of the key selling points of OPV [13]. Perhaps equally important to the processing speed is the lack of complexity. There are many excellent publications demonstrating surface texturing (often at the sub 10-micron scale) of surfaces for a similar end goal [19, 37–40]. Many processes used for this can be time-consuming when compared to the laser process and are certainly more complicated than the "point and shoot" approach of industrial laser usage. The high levels of scattering observed here also demonstrate that complex nanostructures are unnecessary for the production of highly light scattering surfaces. This process can also be completely chemical-free, which offers the opportunity for both production savings and increased safety with the removal of potentially toxic chemicals from the production line. By texturing PET, the ability to improve highly novel forms of PV that use flexible polymer substrates has been demonstrated. Although a contender for this role, PET is not always the substrate used for flexible applications. It does, however, behave comparably to several other transparent polymer materials when irradiated with a CO_2 laser source making it a useful reference material. Indeed, there is evidence in the literature of CO_2 laser processing and/or machining of other polymers that are considered of importance as potential substrates for PV technologies including polyimide and polydimethylsiloxane [41–45].

Another important factor to consider is the effect the process may have on the transparent conducting layers (typically oxides like indium doped tin oxide, TCOs, or polymer mixtures like PEDOT:PSS, TCPs) that coat the substrate. These highly conductive layers act as the front contact of the PV device and as such are vital to attaining high levels of cell performance. The morphology of the organic films

in an OPV cell has a significant effect on cell properties. For example, thicker films, whilst naturally absorbing a greater portion of the incident light, may lead to increased series resistance within the cell, and voids or other defects can increase the likelihood of short circuits leading to a reduction in the shunt resistance (both effects resulting in a reduced cell fill factor) [46–48]. A potential issue could be adverse heat transfer from the PET substrate to the TCO/TCP layer, caused by the laser process, distorting the layer and causing an increase in defects where the organic layer meets the front contact. Whilst this does have the potential to cause problems, these should be minor for two key reasons. Firstly, the processing takes place on the external facing side of the PET substrate and only the more extreme end of the processing conditions tested within this work also affects the internal side (see relative feature size on the inset surfaces on Figures 1–3). Secondly, the conductive coating can be applied after the PET has been laser processed. This would allow for an even TCO/TCP layer to be applied, reducing the likelihood of introducing microshorts. There is also the possibility of gaining a potentially advantageous texturing to the TCO/TCP layer through a templating effect, as it has been demonstrated in the past that texturing of or adding scattering centres into these layers can result in enhanced photon capture and/or superior junction formation, albeit primarily on glass substrates [46–49]. In order to adequately test this, further studies into processing precoated substrates and on coating pretextured substrates are required.

4. Conclusions

This paper has demonstrated a high-speed, simple, and chemical-free method for the production of highly light scattering surfaces for use in flexible PV applications. The parameters of laser power and scanning speed have the largest effect on the level of haze a textured surface produces. It has been observed that at higher powers and slower scanning speeds, there is significantly reduced trapping of air pockets, which is likely due to slower cooling allowing more time for air to escape. Films exhibit an increase in valleys, demonstrated by negative S_{sk} values, which can be considered as very large roughness features due to the high S_{ku}. S_a and S_z values demonstrate that when spacing gets to levels close to those of the spot size, heat transfer/remelting occurs which results in smaller feature sizes. The roughness values do not directly relate to the scattering of light, indicating that the light scattering is more dependent on feature size than explicit microroughness. The light scattering occurs in a direction perpendicular to the direction of the processed laser lines, allowing for the potential for directional applications or novel multidirectional structures. Finally, a brief discussion of how this process may result in improved PV cells has been included discussing both the advantages and some potential issues that may be caused and how they may be overcome. The sample that produced the highest measured haze between 400 and 750 nm had a scanning speed of 100 mm/s, a spacing of 400 μm, and a laser power of 15%. The next step in realising this technological approach to enhanced PV devices requires extensive modelling of the light scattering and testing on functional PV devices.

Data Availability

The data used to support the findings of this study are included within the article.

Conflicts of Interest

The authors declare that there is no conflict of interest regarding the publication of this paper.

Acknowledgments

The authors would like to thank the members of the Faculty of Science and Engineering at the University of Chester for useful conversations whilst undertaking this work, particularly the members of the departments of Natural Sciences and Mechanical Engineering. The work performed here was funded internally through the University of Chester.

References

[1] REN21, *Renewables 2018: Global Status Report*, REN21 Secretariat, Paris, 2018.

[2] M. A. Green, Y. Hishikawa, E. D. Dunlop, D. H. Levi, J. Hohl-Ebinger, and A. W. Y. Ho-Baillie, "Solar cell efficiency tables (version 52)," *Progress in Photovoltaics*, vol. 26, no. 7, pp. 427–436, 2018.

[3] W. Shockley and H. J. Queisser, "Detailed balance limit of efficiency of p-n junction solar cells," *Journal of Applied Physics*, vol. 32, no. 3, pp. 510–519, 1961.

[4] V. Fthenakis, "Sustainability of photovoltaics: the case for thin-film solar cells," *Renewable & Sustainable Energy Reviews*, vol. 13, no. 9, pp. 2746–2750, 2009.

[5] J. F. Yang, Y. Feng, R. Patterson, S. Huang, S. Shrestha, and G. Conibeer, "Theoretical investigation of plasmon enhanced optically-coupled hot carrier extraction," in *2015 IEEE 42nd Photovoltaic Specialist Conference (PVSC)*, New Orleans, LA, USA, 2015.

[6] S. D. Hodgson, G. Kartopu, S. L. Rugen-Hankey, A. J. Clayton, V. Barrioz, and S. J. C. Irvine, "Accessing the quantum palette: quantum-dot spectral conversion towards the BIPV application of thin-film micro-modules," *Journal of Optics*, vol. 17, no. 10, p. 105905, 2015, no. 105905.

[7] M. Yamaguchi, T. Takamoto, K. Araki, and N. Ekins-Daukes, "Multi-junction III-V solar cells: current status and future potential," *Solar Energy*, vol. 79, no. 1, pp. 78–85, 2005.

[8] V. M. Andreev, V. A. Grilikhes, V. P. Khvostikov et al., "Concentrator PV modules and solar cells for TPV systems," *Solar Energy Materials and Solar Cells*, vol. 84, no. 1–4, pp. 3–17, 2004.

[9] M. Gratzel, "Recent advances in sensitized mesoscopic solar cells," *Accounts of Chemical Research*, vol. 42, no. 11, pp. 1788–1798, 2009.

[10] M. M. Lee, J. Teuscher, T. Miyasaka, T. N. Murakami, and H. J. Snaith, "Efficient hybrid solar cells based on meso-superstructured organometal halide perovskites," *Science*, vol. 338, no. 6107, pp. 643–647, 2012.

[11] M. A. Green, A. Ho-Baillie, and H. J. Snaith, "The emergence of perovskite solar cells," *Nature Photonics*, vol. 8, no. 7, pp. 506–514, 2014.

[12] A. Isakova and P. D. Topham, "Polymer strategies in perovskite solar cells," *Journal of Polymer Science Part B: Polymer Physics*, vol. 55, no. 7, pp. 549–568, 2017.

[13] J. E. Carle and F. C. Krebs, "Technological status of organic photovoltaics (OPV)," *Solar Energy Materials and Solar Cells*, vol. 119, pp. 309-310, 2013.

[14] I. M. Peters, H. Hauser, N. Tucher, and B. Blasi, "Optical modeling of honeycomb textures for multicrystalline silicon solar cells," *IEEE Journal of Photovoltaics*, vol. 6, no. 6, pp. 1480–1487, 2016.

[15] H. Melkonyang, S. Saylan, A. Heidelberg et al., "Submicron texturing for broadband light management in thin-film PV," in *Proceedings Volume 8823, Thin Film Solar Technology V*, vol. 8823, p. 2013, San Diego, CA, USA, 2013.

[16] S. Kontermann, T. Gimpel, A. L. Baumann, K. M. Guenther, and W. Schade, "Laser processed black silicon for photovoltaic applications," *Energy Procedia*, vol. 27, pp. 390–395, 2012.

[17] M. Batmunkh, T. J. Macdonald, W. J. Peveler et al., "Plasmonic gold nanostars incorporated into high-efficiency perovskite solar cells," *ChemSusChem*, vol. 10, no. 19, pp. 3750–3753, 2017.

[18] G. Zhang, S. Finefrock, D. Liang et al., "Semiconductor nanostructure-based photovoltaic solar cells," *Nanoscale*, vol. 3, no. 6, pp. 2430–2443, 2011.

[19] D. J. Rogers, V. E. Sandana, S. Gautier et al., "Core–shell GaN–ZnO moth-eye nanostructure arrays grown on a-SiO_2 /Si (1 1 1) as a basis for improved InGaN-based photovoltaics and LEDs," *Photonics and Nanostructures - Fundamentals and Applications*, vol. 15, pp. 53–58, 2015.

[20] T. E. Lizotte and T. R. Okeeffe, "Chemical free cleaning using excimer lasers," *Conference on Lasers as Tools for Manufacturing of Durable Goods and Microelectronics*, 1996, pp. 279–287, San Jose, Ca, USA, 1996.

[21] P. Waurzyniak, "Laser cutting and welding technologies advance," *Manufacturing Engineering*, vol. 147, no. 2, p. 69, 2011.

[22] A. Gillett, D. Waugh, J. Lawrence, M. Swainson, and R. Dixon, "Laser surface modification for the prevention of biofouling by infection causing Escherichia coli," *Journal of Laser Applications*, vol. 28, no. 2, article 022503, 2016.

[23] R. Narayan and P. Goering, "Laser micro- and nanofabrication of biomaterials," *MRS Bulletin*, vol. 36, no. 12, pp. 973–982, 2011.

[24] Y. Cheng, K. Sugioka, and K. Midorikawa, "3D integration of microoptics and microfluidics in glass using femtosecond laser direct writing," in *Proceedings SPIE 5662, Fifth International Symposium on Laser Precision Microfabrication*, Nara, Japan, October 2004.

[25] R. Cristescu, G. Socol, I. N. Mihailescu et al., "New results in pulsed laser deposition of poly-methyl-methacrylate thin films," *Applied Surface Science*, vol. 208-209, pp. 645–650, 2003.

[26] U. Bielesch, J. Uhlenbusch, and W. Viol, "Q-switched low pressure CO2 laser," in *Proceedings Volume 2502, Gas Flow and Chemical Lasers: Tenth International Symposium*, pp. 31–37, Friedrichshafen, Germany, 1995.

[27] T. Sakai and N. Hamada, "A high-power Q-switchedco2laser using intense pulsed RF discharge excitation," *Japanese Journal of Applied Physics*, vol. 35, Part 1, No. 6A, pp. 3428–3435, 1996.

[28] A. K. Dubey and V. Yadava, "Laser beam machining - a review," *International Journal of Machine Tools and Manufacture*, vol. 48, no. 6, pp. 609–628, 2008.

[29] D. E. Duvall, "Environmental degradation of pet and its potential effect on long-term mechanical-properties of oriented pet products," *Polymer-Plastics Technology and Engineering*, vol. 34, no. 2, pp. 227–242, 1995.

[30] S. Ebadian and P. Servati, "Reducing the roughness of transparent electrodes in organic photovoltaic devices on plastic substrate by PEDOT:PSS treatment," *2009 IEEE Nanotechnology Materials and Devices Conference*, 2009, pp. 221–224, Traverse City, MI, USA, June 2009.

[31] C. Roldán-Carmona, O. Malinkiewicz, A. Soriano et al., "Flexible high efficiency perovskite solar cells," *Energy & Environmental Science*, vol. 7, no. 3, pp. 994–997, 2014.

[32] G. Oreski and G. M. Wallner, "Aging mechanisms of polymeric films for PV encapsulation," *Solar Energy*, vol. 79, no. 6, pp. 612–617, 2005.

[33] J.-m. Liu, X.-l. Chen, J. Fang, Y. Zhao, and X.-d. Zhang, "High-haze and wide-spectrum hydrogenated MGZO TCO films on micro-textured glass substrates for thin-film solar cells," *Solar Energy Materials and Solar Cells*, vol. 138, pp. 41–50, 2015.

[34] A. Hongsingthong, T. Krajangsang, A. Limmanee, K. Sriprapha, J. Sritharathikhun, and M. Konagai, "Development of textured ZnO-coated low-cost glass substrate with very high haze ratio for silicon-based thin film solar cells," *Thin solid films*, vol. 537, pp. 291–295, 2013.

[35] K. Li, Y. Zhang, H. Zhen et al., "Versatile biomimetic haze films for efficiency enhancement of photovoltaic devices," *Journal of Materials Chemistry A*, vol. 5, no. 3, pp. 969–974, 2017.

[36] P. Vincent, D. S. Song, H. B. Kwon et al., "Towards maximizing the haze effect of electrodes for high efficiency hybrid tandem solar cell," *Applied Surface Science*, vol. 432, pp. 262–265, 2018.

[37] M. G. Salvaggio, R. Passalacqua, S. Abate et al., "Functional nano-textured titania-coatings with self-cleaning and antireflective properties for photovoltaic surfaces," *Solar energy*, vol. 125, pp. 227–242, 2016.

[38] C. Trompoukis, A. Herman, O. El Daif et al., "Enhanced absorption in thin crystalline silicon films for solar cells by nanoimprint lithography," in *Proceedings Volume 8438, Photonics for Solar Energy Systems IV*, Brussels, Belgium, 2012.

[39] Y. F. Liu, G. J. Blayney, and O. J. Guy, "Rapid microwave growth of ZnO nanowires for low cost photovoltaics cells using reclaimed silicon substrates," in *2012 IEEE International Conference on Electron Devices and Solid State Circuit (EDSSC)*, Bangkok, Thailand, December 2012Chulalongkorn Univ.

[40] K. Watanabe, T. Inoue, H. Sodabanlu, M. Sugiyama, and Y. Nakano, "Thin-film solar cells with InGaAs/GaAsP multiple quantum wells and a rear surface etched with light trapping micro-hole array," *Japanese Journal of Applied Physics*, vol. 54, no. 8S1, article 08KA13, 2015.

[41] K. Znajdek, M. Sibinski, A. Strakowska, and Z. Lisik, "Polymer substrates for flexible photovoltaic cells application in personal electronic system," *Opto-Electronics Review*, vol. 24, no. 1, 2016.

[42] X. Jin, D. Zhu, J. Liu, and X. Zeng, "Mechanism and process of fabricating fluorinated polyimide optical waveguide by CO_2 laser direct-writing," *Optical and Quantum Electronics*, vol. 43, no. 11–15, pp. 163–174, 2012.

[43] K. Coupland, P. R. Herman, and B. Gu, "Laser cleaning of ablation debris from CO_2-laser-etched vias in polyimide," *Applied Surface Science*, vol. 127-129, pp. 731–737, 1998.

[44] B. A. Fogarty, K. E. Heppert, T. J. Cory, K. R. Hulbutta, R. S. Martin, and S. M. Lunte, "Rapid fabrication of poly(dimethylsiloxane)-based microchip capillary electrophoresis devices using CO_2 laser ablation," *The Analyst*, vol. 130, no. 6, pp. 924–930, 2005.

[45] M. T. Khorasani and H. Mirzadeh, "Laser surface modification of silicone rubber to reduce platelet adhesion in vitro," *Journal of Biomaterials Science, Polymer Edition*, vol. 15, no. 1, pp. 59–72, 2004.

[46] J. Xu, Z. Hu, K. Zhang, L. Huang, J. Zhang, and Y. Zhu, "Enhancement in photocurrent through efficient geometrical light trapping in organic photovoltaics," *Energy Technology*, vol. 4, no. 2, pp. 314–318, 2016.

[47] R. M. Howden, E. J. Flores, V. Bulovic, and K. K. Gleason, "The application of oxidative chemical vapor deposited (oCVD) PEDOT to textured and non-planar photovoltaic device geometries for enhanced light trapping," *Organic Electronics*, vol. 14, no. 9, pp. 2257–2268, 2013.

[48] C. Cho, H. Kim, S. Jeong et al., "Random and V-groove texturing for efficient light trapping in organic photovoltaic cells," *Solar energy materials and solar cells*, vol. 115, pp. 36–41, 2013.

[49] Y. Park, L. Muller-Meskamp, K. Vandewal, and K. Leo, "PEDOT:PSS with embedded TiO_2 nanoparticles as light trapping electrode for organic photovoltaics," *Applied Physics Letters*, vol. 108, no. 25, article 253302, 2016.